Research Square

Preprints are preliminary reports that have not undergone peer review.
They should not be considered conclusive, used to inform clinical practice,
or referenced by the media as validated information.

In-situ fault properties and earthquake nucleation revealed by tidal modulation of seismicity

Huiyun Guo

hguo2@caltech.edu

Division of Geological and Planetary Sciences, California Institute of Technology
https://orcid.org/0000-0002-8516-4244

Zachary Ross

California Institute of Technology https://orcid.org/0000-0002-6343-8400

John Wilding

Division of Geological and Planetary Sciences, California Institute of Technology

Jean-Philippe Avouac

Division of Geological and Planetary Sciences, California Institute of Technology
https://orcid.org/0000-0002-3060-8442

Physical Sciences - Article

Keywords:

Posted Date: March 25th, 2026

DOI: https://doi.org/10.21203/rs.3.rs-8991397/v1

License: This work is licensed under a Creative Commons Attribution 4.0 International License.
Read Full License

Additional Declarations: There is **NO** Competing Interest.

In-situ fault properties and earthquake nucleation revealed by tidal modulation of seismicity

Huiyun Guo[1*], Zachary E. Ross[1], John D. Wilding[1], Jean-Philippe Avouac[1,2]

[1]Seismological Laboratory, Division of Geological and Planetary Sciences, California Institute of Technology, Pasadena, 91125, CA, USA.

[2]Division of Engineering and Applied Science, California Institute of Technology, Pasadena, 91125, CA, USA.

*Corresponding author(s). E-mail(s): hguo2@caltech.edu;
Contributing authors: zross@caltech.edu; jwilding@caltech.edu; avouac@caltech.edu;

Abstract

Earthquakes are expected to be sensitive to solid Earth tides [1, 2], yet demonstrating this century old conjecture has been challenging because the signal is damped by the non-instantaneous earthquake nucleation process and can be revealed only with very large earthquake catalogs [3, 4]. Here we demonstrate a clear and statistically significant tidal modulation of seismicity at The Geysers geothermal field in California by constructing a high-resolution catalog of ∼700,000 earthquakes using a deep-learning–based workflow [5–8]. Schuster spectrum analysis of this enhanced catalog reveals pronounced diurnal/semidiurnal peaks aligned with dominant constituents of solid Earth tides, as well as additional peaks at 24-hour and one year associated with geothermal operations. The modulation amplitude from diurnal/semidiurnal solid Earth tides is $\mathbf{3-4\%}$. The tidal modulation amplitude decreases with depth and is enhanced for earthquakes with a higher non-double-couple source component, consistent with a low effective normal stress. The strong sensitivity of seismicity to normal stress perturbations implies a weak coupling between pore-pressure and applied stress and is compatible with a standard friction coefficient of ∼0.5-0.6. The observed tidal signal is consistent with an earthquake nucleation process governed by rate-and-state friction [9], allowing us to derive further constraints on frictional properties of faults and the characteristic timescale of earthquake nucleation under tectonic and geothermal conditions [10–12].

Main

It was conjectured in the 19th century that gravitational forces from the Sun and the Moon deform the solid Earth and therefore, modulate earthquake occurrence [1, 2]. Although solid Earth tidal deformation is well established [13], unambiguous evidence that tides influence earthquake occurrence has emerged only recently [3, 4, 14–18]. This is because the modulation amplitude is small–typically only a few percent–and its detection requires large earthquake catalogs or particular local conditions that enhance the sensitivity to tides [15]. Because tidal stresses are spatially uniform, quasi-static, periodic, and ubiquitous, they provide a simpler and more controlled source of stress perturbation than earthquake interactions or tectonic loading. Hence, sensitivity to tidal stresses can give insight into the earthquake nucleation process [19–21], probing the state of faults relative to failure [16, 22, 23] and the coupling between deformation and fluid pressure [15, 17, 24–27].

Efforts to detect tidal modulation of earthquakes have yielded mixed results to date. While tremors and low frequency earthquakes (LFEs) often show strong correlation with tides [28–32], the sensitivity of ordinary earthquakes to tides is less clear. Earthquakes in shallow subduction zones and mid-ocean ridges have been shown to be sensitive to ocean tides [4, 14, 33–36]. In contrast, for tectonic regions located inland and away from the coast, tidal triggering is hardly detectable using traditional earthquake catalogs [16, 17, 24, 26, 27, 37], except in some volcanic and geothermal areas where tidal triggering appears enhanced [15, 26, 34, 38]. The assortment of works on this topic shows that tidal triggering is highly context-dependent, with detectability largely controlled by the local state of stress and pore-pressure conditions on active faults. Subtle periodic signals can be obscured by nonstationary seismicity rates or anthropogenic noise, while the response itself also depends on faulting style and proximity to failure [39]. The central question therefore remains whether small periodic stresses measurably modulate ordinary seismicity and, if so, how such modulation can constrain the earthquake nucleation process and source properties.

A key missing element is unambiguous tidal modulation in ordinary earthquake sequences combined with connections to the source mechanism. To address this gap, we focus on The Geysers geothermal field (GGF), the world's largest geothermal field in northern California, where decades of sustained power production have produced intense seismicity strongly correlated with injection (Fig.1a) [39–42]. The exceptional density of observations at GGF makes it a prime site to investigate the response of ordinary earthquakes to tides [27]. To evaluate the role of solid Earth tides in modulating inland seismicity and to probe the underlying triggering mechanism of such small stress perturbations, we used deep-learning algorithms to reprocess the continuous seismic waveforms and build a high-resolution earthquake catalog with improved magnitude completeness and locations.

Tidal triggering at The Geysers geothermal field

Our enhanced earthquake catalog contains notable ∼691,000 events spanning 12.8 years (Fig.1a). Most earthquakes are induced by injection activity and exhibit a clear temporal correlation with injection rates (Fig.1c) [39], with only 22% identified as clustered events (Extended Data Fig.1). Seismicity is concentrated between the surface and 5 km depth and clusters spatially around the operational wells of the geothermal field (Fig.1a,b). The spatial pattern also outlines the steam reservoir and associated fluid conduits, with the main reservoir extending from 1 to 4 km depth [43, 44]. Long-term production and cold-water injection at GGF have promoted rapid fluid flow accompanied by crack opening, causing a component of motion perpendicular to the faults and a local volume change [45–48].

We use the declustered catalog and the Schuster test [2] to identify possible periodicities in earthquake occurrence. We calculate the Schuster spectrum [49] which scans different temporal periods and quantifies whether the observed modulation exceeds that expected from a Poisson process. The spectrum reveals a pronounced annual modulation (Fig.2a), most likely reflecting seasonal stress changes associated with variations in injection rates [39, 40, 50]. At periods larger than about one month, the spectrum shows a drift toward low p-values (indicating a low probability that the observed modulation is due to chance). This is a typical feature of an imperfect declustering [49], but the value at one year is well above these spurious values and can be considered very significant. At shorter periods, the spectrum also displays statistically significant peaks at diurnal and semidiurnal constituents of solid Earth tides (Fig.2b), including the semidiurnal M_2 (∼12.42 h), S_2 (∼12 h) and the diurnal K_1 (∼23.93 h) and O_1 (∼25.82 h) constituents. Statistical power is tightly concentrated at these tidal periods and is clearly separated from a 24-hour peak which is most likely associated with daily operational cycle. These observations demonstrate that solid Earth tides significantly modulate the timing of earthquakes at GGF. Converting the constituent-specific Schuster $p-$value to modulation amplitude [49] yields percent-level variations of order 2.96%, 1.55%, 1.81% for M_2, K_1 and O_1, respectively, indicating a small but significant tidal modulation of the seismicity rate.

Tidal triggering is also evident in the distribution of tidal phases, defined as the distribution of earthquake occurrence times within the tidal cycle computed from the combined tidal constituents [14, 49]. If periodic loading influences event times, the distribution will deviate from uniformity, which confirms a significant tidal triggering (Extended Data Fig.2). Because volumetric stress is orientation independent and directly reflects effective normal–stress variations, we adopt tidal phases of volumetric stress as our primary reference. The averaged duration of decreasing peak stress (from high tide to low tide) is slightly longer than that of increasing peak stress, likely due to the complex gravitational interactions among the Earth, Moon, and Sun [34]. We therefore apply a bias-corrected tidal phases to account for the nonuniform phase distribution of the

reference signal [32, 34]. After correction, the phase distribution follows a clean sinusoid with an amplitude of 0.039 and a phase close to 0° (Extended Data Fig.2b), indicating a fractional swing of the instantaneous rate of about ±3.9% at diurnal/semidiurnal periods. We also compute the tidal phase for both normal and shear stresses resolved onto the two dominant fault sets (Extended Data Fig.2c-f) that represent the primary local fault orientations and slip directions [41, 51, 52]. Although normal and shear stresses are intrinsically correlated, it is common practice to assess their effects separately in tidal triggering studies [15, 24, 28]. For simplicity, we assume vertical faults, striking $N30°E$ and $N80°E$. The tidal phase distributions for normal stress on both fault planes closely track those derived from volumetric stresses, indicating that normal stress variations predominantly controls the seismicity response. In contrast, the response to tidal shear stress perturbations is comparatively weaker yet still robust.

Taken together, the spectral and phase-based analyses suggest that solid Earth tides modulate the seismicity rate at GGF by $3-4\%$ over the analysis interval. The abundance of data provided by the enhanced catalog enables the detection of tidal triggering at the few-percent level and the isolation of narrow, constituent-concentrated signals at the tidal periods that would otherwise be obscured by noise. By linking tidal modulation to seismicity, the observed amplitude and phase responses provide constraints on the effective normal stress and rate-and-state friction parameters that govern the seismicity sensitivity to small stress perturbations. To investigate the physical mechanism underlying the observed modulation, we compare these observations with the predicted modulation based on an earthquake nucleation model.

Fault frictional properties and earthquake nucleation timescale

It is already well understood that the weak sensitivity of ordinary earthquakes to tidal stresses implies a non-instantaneous earthquake nucleation process [19]. Such non-instantaneous nucleation is predicted by rate-and-state friction [9], which also provides a possible explanation for the decay rate of aftershocks [10, 53]. Rate-and-state models have also been shown to well-explain the seismicity response to stress variations driven by waste water injection [54, 55] or gas production [21]. We therefore adopt this framework and assume that the geothermal operations and tectonic loading produce a background seismicity rate that is modulated by tidal stress variations. The nucleation process in rate-and-state friction is dependent on the frictional properties and the stressing rate [10], implying that the amplitude and phase of the modulated seismicity rate in response to a periodic stress perturbation depends on the period of the perturbation [10, 20]. Accordingly, we use the Schuster spectrum which provides constituent-specific modulation amplitudes, rather than the analysis based on tidal phase distributions which integrates across multiple frequencies.

We compute Schuster spectra from synthetic catalogs generated under solid Earth tides and invert for fault properties including the rate-and-state friction parameter $A\sigma_0$, the background shear stressing rate $\dot{\tau}$, and an apparent instantaneous friction coefficient μ (Methods). Because the model response is nonlinear, modulation at different forcing periods is not independent [12] and need to be evaluated jointly. We therefore also include the 24-hour operational forcing as a harmonic perturbation with unknown amplitude. Using the best-fitting parameters, the synthetic Schuster spectrum reproduces the principal features of the observation, including a dominant semidiurnal M_2 peak, clear power at O_1, and a distinct 24-hour operational peak (Fig.3a). The model overpredicts the power at K_1 and S_2. This mismatch may reflect the neglected atmospheric loading, which can have strong variability near the K_1 and S_2 frequencies [56] or interference with operational cycles that reduces the apparent tidal power relative to our simplified model for these two constituents.

The observed and synthetic Schuster spectra from the synthetic catalogs are closely consistent (Fig.3a). To assess phase consistency, we compare Schuster walks for the dominant tidal constituents (Fig.3c). The synthetic and observed walks align near phase 0°, defined as the time of peak constituent-specific volumetric stress. For reference, we also show the timing of maximum shear stress resolved on faults striking $N30°E$ and $N80°E$. Seismicity is better in phase with the peak volumetric stress, so that it is in phase with the minimum normal stress, suggesting that seismicity is favored by unclamping and indicating a non-negligible friction. This inference is consistent with the phase analysis which shows substantially stronger modulation with normal stress than with shear stress perturbations (Extended Data Fig.3). We therefore conclude that (1) the seismicity is primarily modulated by normal stress variations, implying that friction is not negligible, and (2) the response is inconsistent with instantaneous nucleation, in which seismicity would peak at the maximum stressing rate rather than at peak stress [19, 20, 32].

Consistent with this qualitative assessment, the inversion yields a best-fitting friction coefficient of $\mu \sim 0.54$ (Fig.3b), comparable to rock friction coefficients measured in laboratory experiments [57]. A trade-off exists between μ and $A\sigma_0$ because the Coulomb stress change ($S = \tau - \mu\sigma$) involves the product of normal stress and friction coefficient. However, this trade-off is partially mitigated by the fact that shear stress changes also affect the seismicity while variations in shear stress and normal stress are out of phase. As a result, the inversion excludes friction coefficient lower than 0.3 and $A\sigma_0$ values below 5 kPa at the 1-σ confidence level. We estimate the best-fitting $A\sigma_0$ to be approximately 9.8 kPa. Laboratory measurements indicate that A typically ranges from $10^{-3} - 10^{-2}$ for different types of rocks and fault gouges [57, 58], implying the initial normal stress at GGF of $\sim 0.98 - 9.8$ MPa. This estimate is consistent with the local pressure from operation reports [59, 60] and remains well below hydrostatic pressure at the corresponding depths, indicating a very weak crust at GGF. The background stressing rate $\dot{\tau}$ is less well constrained and

spans roughly two orders of magnitude (Extended Data Fig.4), possibly reflecting heterogeneous loading due to the thermoporoelastic effects associated with cold-water injection and steam extraction superimposed on tectonic loading.

Together, $A\sigma_0$ and $\dot{\tau}$ set the characteristic nucleation time, $t_a = A\sigma_0/\dot{\tau}$. Using a representative long-term tectonic stressing rate of 30 kPa/yr [61], we estimate $t_a \approx 120$ days under tectonic loading, one or two orders of magnitude shorter than values typically inferred from laboratory friction assuming hydrostatic pore-pressure [10, 19]. Such a short nucleation timescale explains why the sensitivity of ordinary earthquakes to seasonal loading is detectable in standard seismicity catalogs [17, 62]. In contrast, the response of ordinary earthquakes to solid Earth tides is damped because t_a, under purely tectonic loading, is much larger than the periods of the dominant tidal constituents. Under geothermal conditions, however, the sensitivity to solid Earth tides is enhanced due to higher stressing rates and possibly lower effective normal stress associated with geothermal operations. Both effects reduce t_a relative to purely tectonic loading.

Comparison with tidal modulation of low frequency earthquakes

It is instructive to compare the tidal sensitivity of ordinary earthquakes at GGF with that of LFEs. Prior observations have shown that LFEs exhibit little sensitivity to normal stress variations associated with tides [28, 30, 32]. LFEs typically occur under undrained and saturated conditions, where fluid pressure appraches lithostatic pressure with strong coupling between pore-pressure and normal stress with a Skempton's coefficient $B \sim 1$, so that normal stress variations are compensated by pore-pressure variations [28, 32]. Consequently, the apparent friction coefficient inferred from tidal modulation of LFEs approximates the instantaneous friction coefficient $\mu * (1 - B)$ and is therefore very small ($\mu \approx 0.02$–0.06) [28, 32, 63]. In contrast, ordinary earthquakes at GGF are sensitive to tidal normal stress variations, as shown here and previously reported [27]. The inferred apparent friction coefficient for ordinary earthquakes ($\mu \approx 0.54$) is significantly higher than that for LFEs, indicating a fundamental difference in how tidal stresses influence effective normal stress and pore-pressure. Laboratory studies suggest that while the intrinsic friction coefficient of rocks is relatively stable [64], the instantaneous frictional response relevant for triggering depends on the evolving effective normal stress, which is controlled by pore-pressure conditions and poroelastic coupling efficiency [65–67]. In porous and partially saturated media, poroelastic coupling governs the transmission of external stress perturbations to the fault through induced pore-pressure changes [67]. In fluid-rich and saturated environments, such as those hosting LFEs, strong pore-pressure coupling reduces effective normal stress and enhances tidal seismicity. By contrast, in hot, drained conditions (i.e., GGF), limited fluid compressibility and rapid thermal diffusion may suppress pore-pressure increases tidal timescales. Under these

conditions, normal stress perturbations contribute more directly to Coulomb stress changes and the apparent coefficient of friction can be measured high because partial saturation leads to negligible coupling between normal stress and pore-pressure ($B \sim 0$) even under undrained conditions [27].

More broadly, tidal triggering of ordinary earthquakes and LFEs reveals fundamental differences in their sensitivities to normal/shear stresses, reflecting contrasting fault environments. LFEs and tremors that exhibit strong tidal modulation typically occur on weak fault interfaces near the brittle–ductile transition, where effective normal stress is low and slow slip can persist over weeks to months [32, 68, 69]. In this regime, small shear stress oscillations are sufficient to modulate the occurrence of LFEs/tremor [31]. These deep, weak faults with very low effective coefficients of friction can have near-lithostatic pore-pressure and are strongly rate-sensitive to tidal loads [28, 31, 32]. In contrast, most ordinary earthquakes occur on stronger, more brittle faults that require larger stress excursions to nucleate. Small periodic stresses therefore remain hidden in background variability unless stress conditions are unusually close to failure [19]. Where effective normal stress is reduced (e.g., in some thrust, volcanic, ridge, or geothermal settings), measurable tidal modulation of ordinary earthquakes is more commonly observed [14, 15, 24, 27, 70]. Thus, tidal sensitivity appears to be primarily controlled by effective normal stress, with rate–and–state friction providing a quantitative framework linking small oscillatory stresses to seismicity-rate variations [10, 12, 32].

Earthquake source tensor control of tidal modulation

Earthquake sources at GGF have significant non-double-couple (NDC) components, consistent with fault slip accompanied by fluid pressurization or thermal contraction [39, 40, 50, 71]. The resulting low effective normal stress then contribute to the significant sensitivity of ordinary earthquakes to tides at GGF and other geothermal fields. To test this hypothesis, we examine whether tidal modulation amplitude correlates with the fraction of the NDC component.

We determine full moment tensors for 35,115 earthquakes whose solutions are well represented by the two fault planes assumed in the modeling (Supplentary Fig.6). Focal mechanisms vary with depth, transitioning from predominantly strike-slip faulting at shallow levels to more extensional within the reservoir and reverting toward strike-slip at deeper depth (Extended Data Fig.5). When projected onto the moment tensor lune diagram by depth (Fig.4a), most solutions are dominated by shear (double-couple) motion with a persistent tensile component. With increasing depth, the solutions concentrate into a largely unimodal cluster on the lune with diminished scatter toward the isotropic (ISO) and compensated linear vector dipole (CLVD) regions, indicating shear-dominated sources accompanied by a deviatoric source with persistent volumetric

dilation. Overall, faulting within this geothermal reservoir is primarily shear with a superimposed tensile-opening component [46, 48].

As tidal triggering is sensitive to the local stress state [27], we investigate how modulation amplitude varies with depth-dependent source characteristics, focusing on its possible correlation with the NDC fraction. Modulation amplitudes are derived from tidal phases computed using volumetric stress, noting that alternative stress metrics yield similar trends (Extended Data Fig.2). We apply sliding windows of various sizes, shifting every 10,000 events to quantify depth dependence, and fit a diurnal/semidiurnal tidal model within each window to estimate the modulation amplitude. We observed a systematic decrease in modulation amplitude with depth (Fig.4b). The amplitude shows a strong positive correlation (Pearson $r = 0.915$) with the averaged NDC fraction, defined as $|ISO\%|+|CLVD\%|$ (Fig.4b). Here, the averaged NDC fraction serves not as a measure of geometric fault complexity but as a proxy for the prevailing stress state. Although individual values fluctuate, the long-term average NDC fraction decreases with depth, likely reflecting the suppression of tensile deformation under increasing lithostatic pressure. The observed correlation implies that enhanced tidal sensitivity is associated with tensile components indicative of reduced effective normal stress due to high pore-pressure or thermal stresses. This interpretation is consistent with theoretical predictions that low effective normal stress amplifies the response to periodic stresses and thus enhances tidal modulation sensitivity.

Implications

Although tidal modulation of ordinary earthquakes has been widely discussed, its detectability has remained debated due to limited observational evidence [3, 17, 37]. Our machine-learning–enhanced seismicity catalog and high-quality moment-tensor solutions provide unique insight into how ordinary earthquakes respond to solid Earth tides at GGF. Decades of injection and production have imposed substantial volumetric deformation within a steam reservoir underlain by a long-lived magmatic heat source [40, 43, 45, 47, 72, 73], yielding a tidal triggering mechanism distinct from that of LFEs and rendering the modulation signal particularly clear.

The amplitude and phase of tidal modulation provide constraints on the earthquake nucleation process, pore-pressure and frictional properties that are otherwise difficult to estimate under in-situ conditions. Our analysis shows that the strong sensitivity of seismicity to tidal normal stress variations at GGF is consistent with a standard coefficient of fault friction, consistent with laboratory measurements and unsaturated conditions as expected in the context of the steam-dominated geothermal reservoirs. The enhanced tidal triggering

of ordinary earthquakes at geothermal fields is likely driven by high stressing rate and reduced effective normal stress associated with injection and extraction operations. By combining extensive observations with physics-based modeling, we provide quantitative constraints on nucleation timescales and frictional behavior. These results demonstrate that even small periodic stress perturbations can reveal fundamental fault properties when effective normal stress is sufficiently low and stressing rates are elevated. More broadly, tidal modulation offers a natural, continuously operating stress experiment that can be exploited to probe fault strength, fluid coupling, and earthquake nucleation under both tectonic and anthropogenic forcing conditions.

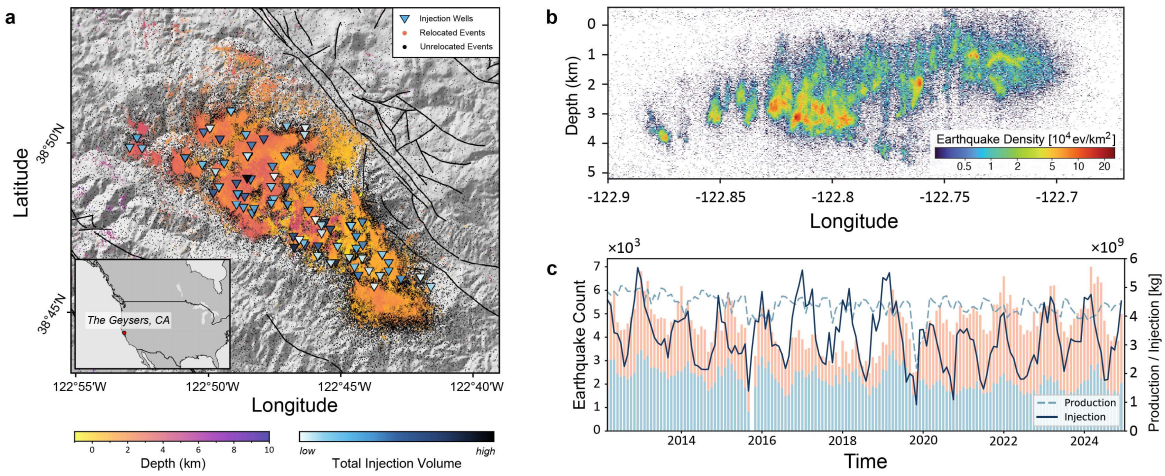


Fig. 1 Seismicity at The Geysers geothermal field.
a, Map view of the seismicity and injectors at GGF. Relocated earthquakes are colored by depth, and un-relocated earthquakes are colored black. All injection wells are colored by their total injection volume. Steam wells are not shown in this figure as their production volume is not well-related with the earthquake rate. **b**, Seismicity density of the enhanced earthquake catalog. **c**, Monthly seismicity rate, injection rate from injection wells and production rate from steam wells in time. Coral bars include all detected earthquakes while blue bars only show the relocated, non-clustered events that are used for the following analysis. Injection rate is marked by dark blue line and production rate is marked by dashed light blue line. Gap in 2015 for the seismicity rate is caused by missing data due to local wildfire.

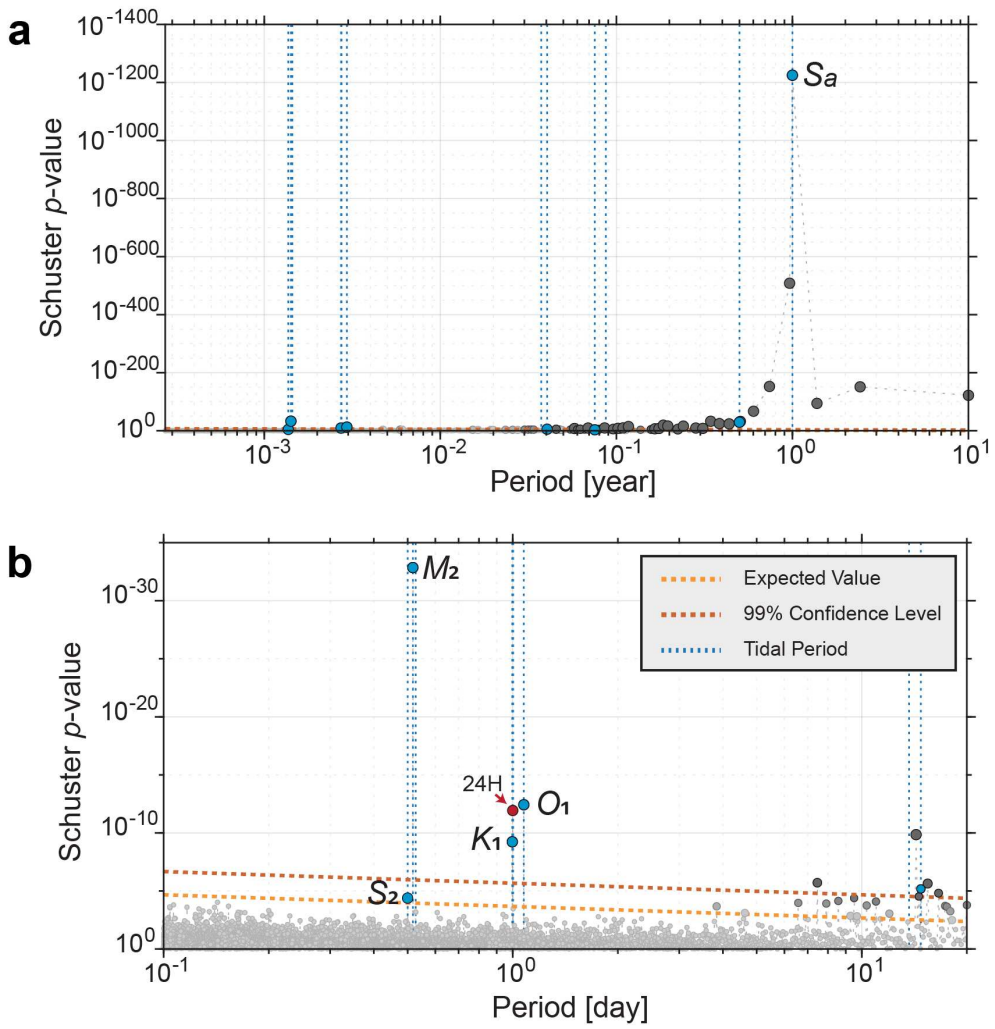


Fig. 2 Schuster spectrum on the enhanced catalog at The Geysers geothermal field.
a, Schuster spectra calculated for periods from 10^{-3} to 10 years. **b**, Schuster spectra calculated for periods from 0.1 to 20 days. The period-dependent "expected value" (orange dashed line) represents the expected minimum Schuster $p-$value while "99% confidence level" (red dashed line) corresponds to 1% of minimum expected values.

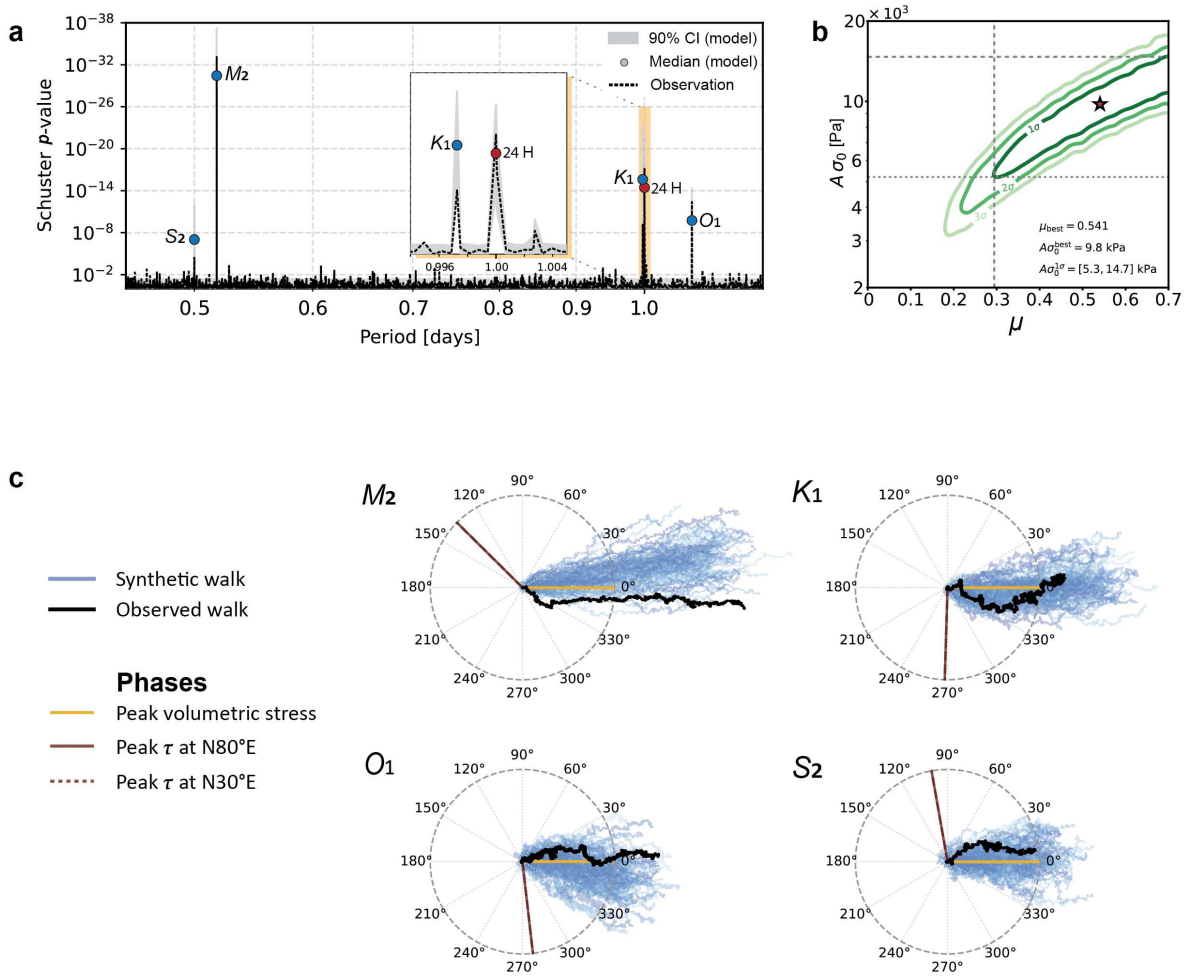


Fig. 3 Synthetic test results under a spring–slider, rate-and-state model.
a, Schuster p-value spectrum as a function of period, where statistically significant periodicities associated with tidal constituents (e.g., M_2, K_1, O_1, and S_2) are labeled. The synthetic result is modeled using the best-fitting parameters. Zoomed-in view shows the diurnal band near 1 day, highlighting the separation between the K_1 and 24 h periods. **b**, Joint χ^2 confidence contours in the (μ, $A\sigma_0$) parameter space. Dark to light green contours denote the 1σ, 2σ, and 3σ confidence levels, respectively, based on $\Delta\chi^2$ thresholds. The red star marks the best-fitting model with $\mu_{\mathrm{best}} = 0.541$ and $A\sigma_0^{\mathrm{best}} = 9.8$ kPa. Dashed lines indicate the 1σ projection range. **c**, Schuster walks for the dominant tidal constituents. Blue lines show synthetic walks from the model ensemble, while black lines represent the observed walks. Radial lines indicate the phases of peak volumetric stress and peak shear stresses resolved along orientations of N80°E and N30°E.

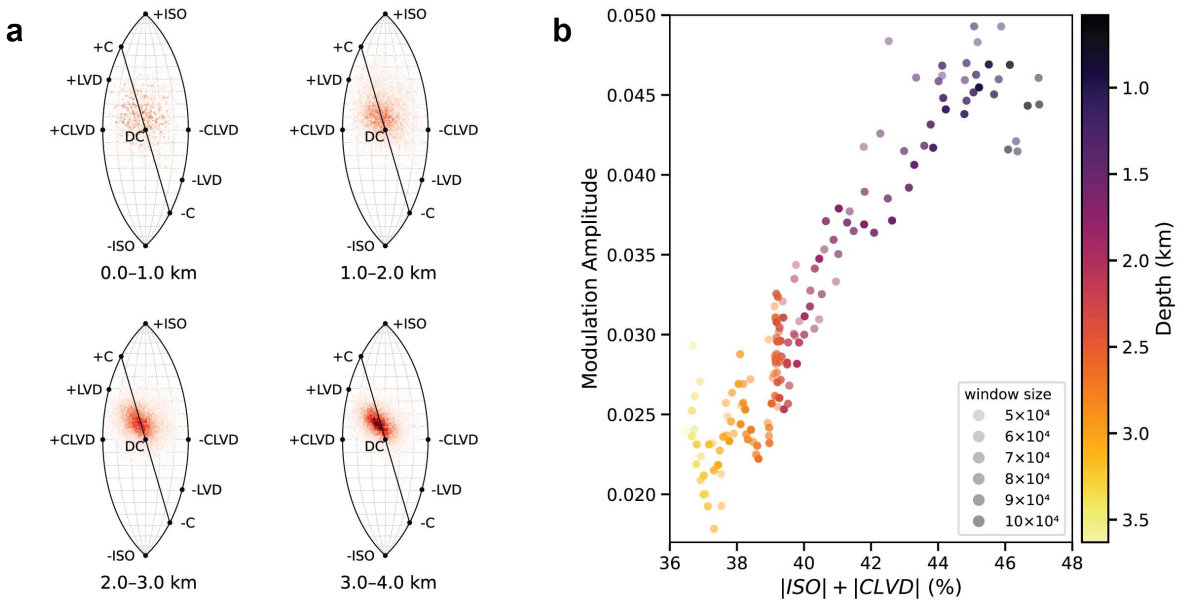


Fig. 4 Illustration of the tidal modulation analysis.
a, Illustration of non-double-couple components on the lune diagram, varying by depth. **b**, Modulation amplitude varying with none-double-couple components. Colors represent depth and transparency of the data points represents the number of earthquakes used in tidal modulation analysis for each depth window.

Methods

Seismicity Catalog Construction

We constructed a high-resolution seismicity catalog for The Geysers geothermal field using a deep-learning–based workflow that includes phase picking, association, earthquake location, waveform cross-correlation, earthquake relocation, and magnitude estimation.

Data. We analyzed nearly thirteen years of continuous waveforms (2012/03/16 to 2024/12/31) from five networks: Northern California Seismic Network (NC), Berkeley Digital Seismic Network (BK), United States National Strong-Motion Network (NP), Plate Boundary Observatory Borehole Network (PB), and the local Berkeley Geysers Network (BG). In total, data from 69 stations were used (Supplementary Fig.1).

Earthquake Detection. We first picked P and S arrivals from the continuous data using the deep-learning picker PhaseNet, yielding ∼21.0 million P and ∼22.1 million S picks [5]. These picks were then associated into events using the high-throughput associator PyOcto with a local velocity model [6, 43], grouping ∼10.8 million P and ∼11.3 million S picks into an initial catalog of ∼720k earthquakes.

Earthquake Location. Event locations were computed using HypoSVI, which employs a differentiable Eikonal solver (EikoNet) to evaluate first-arrival travel times and their spatial gradients [7, 74]. Because some stations recorded secondary body-wave multiples within tenths of a second of the first arrivals, we removed spurious picks using station-specific residual thresholds relative to median residuals, thereby improving absolute locations. To further mitigate path-dependent biases from unmodeled 3D structure, we iteratively applied source-specific station terms (SSST) following the shrinking-box formulation, alternately updating station corrections and relocating events [75]. Earthquake depths are referenced to sea level (negative values indicate seismicity above sea level), and station elevations were included in all travel-time calculations.

Earthquake Relocation. To improve relative location accuracy, we measured differential P- and S-wave arrival times by waveform cross-correlation between neighboring events and relocated earthquakes using GlowClust [8]. For each located event, we cross-correlated waveforms with its K nearest neighbors ($K = 100$). The final catalog contains ∼691,602 earthquakes, of which ∼509,917 were successfully relocated. Over the same time span, the enhanced catalog exceeds the size of the ANSS Comprehensive Earthquake Catalog (ComCat) by a factor of ∼4.5 with a recovery rate of 95.94% (Supplementary Fig.2a) [76].

Earthquake Magnitudes. Local magnitudes (M_L) were estimated by referencing Wood–Anderson (WA) amplitudes [77] and invert jointly for geometric spreading, anelastic attenuation, event magnitudes, and

station-specific corrections within a single linear framework [78, 79]. The linear system is assembled from WA peak amplitudes and hypocentral distances for all available event–station pairs, with a zero-mean constraint on station corrections. We solve the overdetermined system using a singular-value–decomposition generalized inverse, which accommodates uneven network coverage and path heterogeneity while producing an internally consistent magnitude scale across the network [80, 81]. The final catalog has an overall magnitude of completeness of ~ -0.28 and a Gutenberg–Richter slope of $b \approx 0.92$ (Supplementary Fig.2b).

Earthquake Declustering

We performed earthquake declustering using the nearest neighbor approach [82], which is based on the spatial and temporal inter-event distances. The rescaled temporal and spatial distances between earthquakes i and j, denoted T_{ij} and R_{ij}, are defined as,

$$T_{ij} = t_{ij} 10^{-qbm_i}, \quad R_{ij} = (r_{ij})^{d_f} 10^{-(1-q)bm_i}. \tag{1}$$

where $t_{ij} = t_j - t_i$ is the inter-event time (positive if earthquake i occurs before event j, and negative otherwise), r_{ij} is the spatial epicentral or hypocentral distance of the two earthquakes, m_i is the magnitude of event i, d_f is the fractal dimension of the earthquake distribution ($d_f \in [1, 2]$ for 2D distribution and $d_f \in [2, 3]$ for 3D distributions), and $q = 0.5$ in this study. The nearest-neighbour distance (NND) between events i and j is then defined as,

$$\eta_{ij} = T_{ij} R_{ij}. \tag{2}$$

Analysis of the observed seismicity reveals a pronounced bimodal distribution in both the (T, R) space and the distribution of η (Extended Data Fig.1). The first mode, distributed above the white diagonal line in Extended Data Fig.1a, is characteristic of a Stationary Homogeneous Poisson process and can be referred as background. The other mode is located closer to the origin in the distribution of η (Extended Data Fig.1b) and has horizontally elongated shape in the (T, R) space (Extended Data Fig.1a), defined as clustered. We then choose a critical distance η_0 based on the distribution of η to separate the clustered ($\eta \geq \eta_0$) and non-clustered ($\eta < \eta_0$) events.

Schuster Test and Schuster Spectrum

We applied the Schuster test following established formulations [2, 49] to test whether earthquake occurrence is periodically modulated at a trial period T. In the Schuster random–walk statistic, each event time t_k is associated to a phase $\theta_k = 2\pi \frac{t_k}{T}$, if the timing of events in a catalog varies according to a sine-wave function

of period T. Under the null hypothesis of a uniform (period–independent) rate, the distance D between the start and end points of the 2D random walk is,

$$D \;=\; \Big|\sum_{k=1}^{N} e^{i\theta_k}\Big|, \tag{3}$$

where N is the number of events in the catalog. The probability p that the resultant random-walk vector has a length at least D is given by,

$$p \;=\; \exp\!\left(-\frac{D^2}{N}\right), \tag{4}$$

which quantifies how unlikely the observed phase clustering is if events are independent of the period T. Small p indicates nonuniform phase, which indicates a periodic modulation at T.

If earthquake occurrence follow a sinusoidally modulated rate of period T, the normalized seismicity rate can be written as,

$$\frac{R(t_k)}{r} \;=\; 1 \;+\; \alpha\cos\!\left(2\pi\,\frac{t_k}{T}\right), \tag{5}$$

where r is the average seismicity rate, α is the amplitude of the seismicity-rate variations. The Schuster $p-$value is independent of the period tested T and only determined by both the number of events N in the catalog and the modulation amplitude α as,

$$\big\langle -\ln p\big\rangle \;=\; \left\langle\frac{D^2}{N}\right\rangle \;=\; 1 \;+\; \frac{N\alpha^2}{4}. \tag{6}$$

Rather than testing a single period in isolation, a Schuster spectrum evaluates the Schuster statistic over a suitably sampled set of trial periods spanning the frequency band of interest. Sampling approximately uniformly in frequency avoids redundant tests and yields a spectrum in which true periodic signals appear as isolated, band-limited minima in $p-$values, whereas nonperiodic or slowly varying rate changes manifest as broad depressions across multiple periods. Because multiple periods are tested, we can interpret peaks against period-dependent detection levels which makes the spectrum a diagnostic tool both for detecting periodicity and for checking whether declustering was sufficient [49].

Tidal Modulation

We compute solid-Earth (and ocean-load) tidal strains with *Some Programs for Ocean – Tide Loading* (SPOTL) including the dominant tidal constituents, M_2, S_2, N_2, K_2, K_1, O_1, P_1, Q_1, M_f, and M_m, such

that the tidal stress time series can be expressed as,

$$\sigma(t) \;=\; \sum_i \sigma_i \cos\big(\omega_i\, t + \theta_i\big), \tag{7}$$

and each constituent can be analyzed separately. At GGF, the absolute normal strain change resolved on the two dominant faults is about five times larger than the corresponding shear strain change (Extended Data Fig.3).

For the phase distribution analysis based on full tides, each event time t_k is mapped to a tidal phase $\theta_k \in (-\pi, \pi]$, where $\theta_k = 0$ corresponds to peak tidal loading. The phase distribution is modeled as a sinusoidal modulation superimposed on a background rate:

$$\frac{P(\theta)}{P_0} \;=\; 1 \;+\; \frac{P_m}{P_0}\, \cos\big(\theta - \varphi\big), \tag{8}$$

where $P_m/P_0 \in [0, 1]$ is the modulation amplitude (equivalent to α in equation(5), equation(6)), and φ is the phase lag.

Because the full tidal signal contains multiple frequency constituents, the reference phase distribution P_0 is intrinsically nonuniform, reflecting asymmetries in loading and unloading durations [34]. To remove this inherent phase bias, we estimated the background probability P_0 using synthetic catalogs with uniformly distributed event times and corrected the observed phase distribution P_m accordingly. Modulation amplitudes are considered significant only if they exceed both the 97.5% expected from a uniform random process and the 97.5% of spurious modulation arising from correlations among stress components [32]. Uncertainties were quantified using Monte-Carlo procedures [83].

Inversion of Fault Properties

We model the seismicity-rate response to stress perturbations using a spring–slider formulation of rate-and-state friction. Assuming that the initial shear stress is independent of source number and that the background normal stress is time invariant, the normalized seismicity-rate response can be written as, [11]:

$$\frac{R(t)}{r} = \frac{K(t)}{1 + \frac{1}{t_a}\int_0^t K(t')\, dt'}, \tag{9}$$

where R is the seismicity rate produced by a population of seismic sources, r is the background seismicity rate as a constant, $t_a = \frac{A\sigma_0}{\dot{\tau}_r}$ is a characteristic time over which fluctuations in seismicity rate return to the

background seismicity, A is a constitutive parameter proportional to the instantaneous frictional dependence on rate, σ_0 is the background effective normal stress, and $\dot{\tau}_r$ is the background shear stressing rate.

In the case of oscillatory stresses, if changes in normal stress $\sigma(t)$ are small compared to the initial normal stress σ_0, then K can be approximated as [12]:

$$K(t) \approx \exp\left(\frac{S(t)}{A\sigma_0}\right). \tag{10}$$

where $S(t) = \tau(t) - \mu\sigma(t)$ is the modified Coulomb stressing history. Here, $\tau(t) = \dot{\tau}_r t + \Delta\tau$ is the sum of the background shear stressing and the tidally induced shear stress, $\sigma(t) = \Delta\sigma$ is the tidally induced normal stress, and $\mu = \tau_0/\sigma_0 - \alpha$ where α is the Linker and Dieterich constant, describing the coupling of normal stress and state, typically between 0 and 0.25 [84]. Notably, μ does not represent a traditional coefficient of friction, but the apparent instantaneous friction coefficient, describing immediate sensitivity of shear strength to changes in normal stress. We consider the Coulomb stress changes on both dominant fault planes from tides as well as a daily pressure change D to model the 24-hour periodicity shown in the Schuster spectrum.

To generate synthetic earthquake catalogs consistent with the time-varying triggering function $R(t)/r$, we model earthquake occurrence as an inhomogeneous Poisson process [85]. The function $R(t)/r$ is interpreted as a normalized modulation of the background seismicity rate, and is rescaled into physical occurrence rates. Specifically, the total instantaneous rate at time t is expressed as,

$$\lambda(t) = \lambda_0 R(t), \tag{11}$$

where λ_0 is a constant background rate of events per unit time. $R(t)$ controls the contribution of the modulation with time. In practice, the catalog is generated over discrete time bins of duration Δt. Within the i^{th} bin, the expected number of events is,

$$U_i = \lambda_i \Delta t, \tag{12}$$

where $\lambda_i = \lambda_0 R_i$. Following the assumption of a Poisson process, the actual number of earthquakes in the i^{th} bin is modeled as a Poisson random variable k_i, with the corresponding probability mass function,

$$P_r(k_i = k) = \frac{U_i^k}{k!} e^{-U_i}, k = 0, 1, 2, ... \tag{13}$$

This procedure accounts for both the deterministic modulation imposed by $R(t)$ and the intrinsic randomness of earthquake occurrence. If $k_i = 0$, no events are placed in that interval; if $k_i > 0$, the event times are randomized uniformly within the bin.

We impose that the total number of events in each synthetic catalog equals that of the declustered observed catalog. For each synthetic catalog, we compute the endpoint of the 2D Schuster random walk that is made of successive unit-length steps in directions given by event phases according to a sine-wave function of period T [49] corresponding to the tidal constituents. Here in our study, T is 0.517525, 1.075805, 0.99727, 0.5, and 1 in the unit of days for tidal constituent M_2, O_1, K_1, S_2, and the daily pressure change, respectively.. Phase 0° corresponds to the timing of peak decomposed volumetric stress for each tidal constituent and to 00:00:00 UTC for the daily operational cycle. Model fitting is performed using a standard grid search to evaluate the reduced chi-square (χ^2) for the ith parameter set, defined as,

$$\chi^2_{red,i}(A\sigma_0, \dot{\tau}, \mu) = \frac{1}{n_f} \sum_{j=1}^{M} \left(\frac{1}{\sigma_i^2} \sum_{k=1}^{N} d_k^2 \right), \tag{14}$$

where n_f is the number of degrees of freedom, d_k is vector distance between observed and the kth synthetic Schuster-walk endpoints, σ_i is the standard deviation of the vector distances for the ith parameter set, M is the number of tested periods, and N is the total number of synthetic catalogs used for each parameter set test.

Confidence intervals are estimated using standard chi-square criteria. At the criteria of fixed D at 700 Pa, we quantify the uncertainty of three unknown model parameters from Schuster walks of four tidal constituents. The degree of freedom n_f is then set to be 1. M is 4 and N is 100 in this study. Our model turns out to be appropriate that does not overfit or underfit with a minimum reduced chi-square of about one for the parameter sets (Extended Data Fig.4). Using chi-square criterion with 1σ confidence interval ($\Delta\chi^2$=3.53 for 3 degrees of freedom) to estimate the uncertainties of the parameters (Fig.3b), we find $A\sigma_0 = 9.8^{+4.9}_{-4.5}$ kPa, $\mu = 0.54^{+0.16}_{-0.25}$, whereas $\dot{\tau}$ is less constrained, ranging from 10 Pa/day to 3000 Pa/day. In Supplementary Fig.5, we solved $A\sigma_0$ and μ separately corresponding to varying $\dot{\tau}$ using the scenario of $\Delta\chi^2$=2.3 for 2 degrees of freedom. With the solved parameters, we estimate the characteristic nucleation time $t_a = \frac{A\sigma_0}{\dot{\tau}} \in [3.6, 950]$ days based on the various background stressing rate.

Moment Tensor Inversion

We solved the moment tensor of 35,115 earthquakes following the workflow described in prior works [86]. We analyzed vertical-component velocity waveforms from 69 stations that were used to build the enhanced

catalog. Instrument responses were removed and signals were converted to displacement. For each event, we computed source spectra and corner frequency of each event with at least 20 P-wave picks [87–89].

We used an automated picker which was designed to avoid emergent onsets to measure the first-swing P-wave from vertical displacement amplitudes [90]. To recover measurements for low signal-noise-ratio (SNR) traces that pass network and timing checks, we implemented a proximity-based rescaling procedure. For a target event–station with a failed pick, we locate nearby events recorded on the same station, band-limit both waveforms to the event-specific passband, cross-correlate within a short window around the P pick, and rescale the high-SNR neighbor waveform to the target before re-measuring the first-swing amplitude [86]. This increases usable observations while preserving station and path characteristics.

We relate observed P-wave amplitudes to the six independent components of the seismic moment tensor and cast the inversion as a Bayesian inference problem [91]. Posterior densities over moment-tensor components are approximated using Stein variational gradient descent (SVGD), which represents the posterior as an ensemble of particles evolved to match the target distribution [92]. To provide robustness to outliers, we adopt a Huber-loss likelihood that behaves quadratically for small residuals and linearly for large residuals [93]. The scale parameter of the Huber density is estimated from the distribution of amplitude residuals after scaling observations and predictions to the focal sphere. It is then event-wise rescaled to reflect predicted amplitude levels.

A source-specific variant of the amplitude-correction scheme was implemented to mitigate unmodeled 3D attenuation and path effect [90]. After an initial inversion, we compute station-wise ratios of predicted to observed amplitudes using local event neighborhoods. These ratios define source- and station-specific correction factors that update measured amplitudes with a small weight, followed by re-inversion. The process iterates until the median absolute deviation (MAD) of amplitude residuals stabilizes, yielding smoothly varying corrections and minimizing edge artifacts associated with arbitrary spatial partitioning. The same framework also flags problematic stations via modeled–observed polarity agreement statistics. All automated picks and rescaled measurements were subject to the amplitude-window and SNR criteria above, and inversions were repeated after each correction iteration. Convergence was declared when the decline in residual MAD plateaued, ensuring internally consistent amplitudes, stable moment tensors, and station corrections [86].

In contrast to the typical reverse and strike-slip faulting types observed in the coast ranges and the San Andreas Fault system in northern California, GGF appears to be characterized by strike-slip faulting, normal faulting, and combinations thereof. The focal mechanism of the earthquakes at GGF can change with depth with a combined strike-slip/normal faulting regime (Extended Data Fig.5). We did not observe clear

transition between strike-slip and normal faulting from the depth-dependent measurements of faulting types like other observations did (Supplementary Fig.7)[47].

Acknowledgements. We thank Roland Burgmann, Zeyan Zhao, Emily Brodsky, John Vidale and Hao Zhang for their constructive discussions. This work is supported by the National Science Foundation (NSF) Grant EAR-2239666 and David and Lucile Packard Foundation.

Ethics Declarations. The authors declare no competing interests.

Data availability. Seismic data are publicly available from the IRIS DMC. The ANSS Comprehensive Earthquake Catalog (ComCat) is available at United States Geological Survey [76]. The catalog and moment tensor solutions are available upon request from the authors.

Code availability. Code for phase detection can be found at https://github.com/AI4EPS/PhaseNet.git. Phase association code is available at https://github.com/yetinam/pyocto.git. Earthquake location code is available at https://github.com/interseismic/eikonet_julia.git. Earthquake relocation code is available at https://github.com/dttrugman/GrowClust.git.

Author contribution. H.G. performed phase picking. H.G., Z.E.R., and J.D.W. performed quality control on the phase picks and constructed the catalog. H.G. and Z.E.R. performed earthquake relocation. H.G. and J.D.W. performed the computation of moment tensors. H.G. and J.A. performed tidal modulation modeling. H.G, Z.E.R., J.D.W., and J.A. contributed to data analysis and writing. All authors contributed to the revised version of the manuscript.

Extended data figures and tables

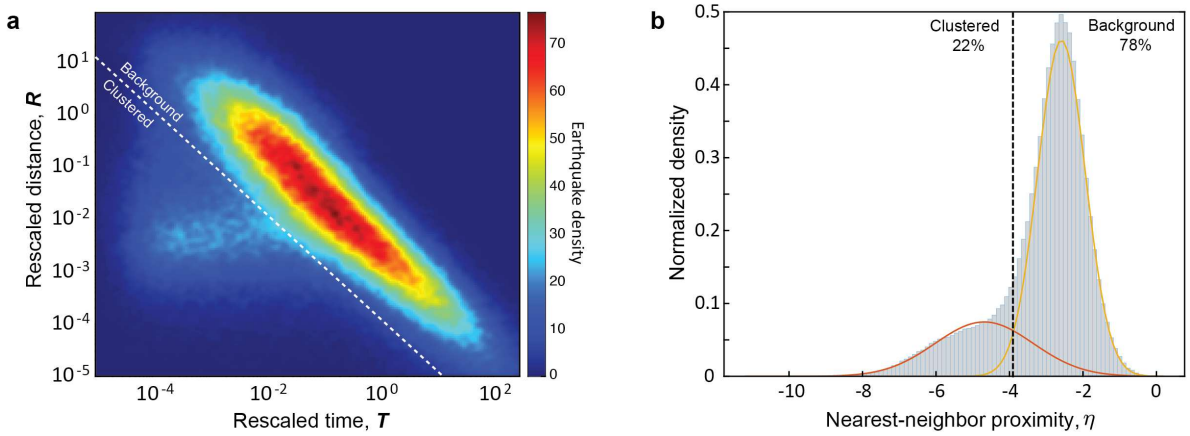


Fig. 1 Earthquake declustering using nearest-neighbor distances.
a, Rescaled distance versus rescaled time for the catalog using a fractal dimension of 1.6. **b**, Probability density of the nearest neighbor distances from panel (a). Clustered events represent $\sim 22\%$ of the catalog.

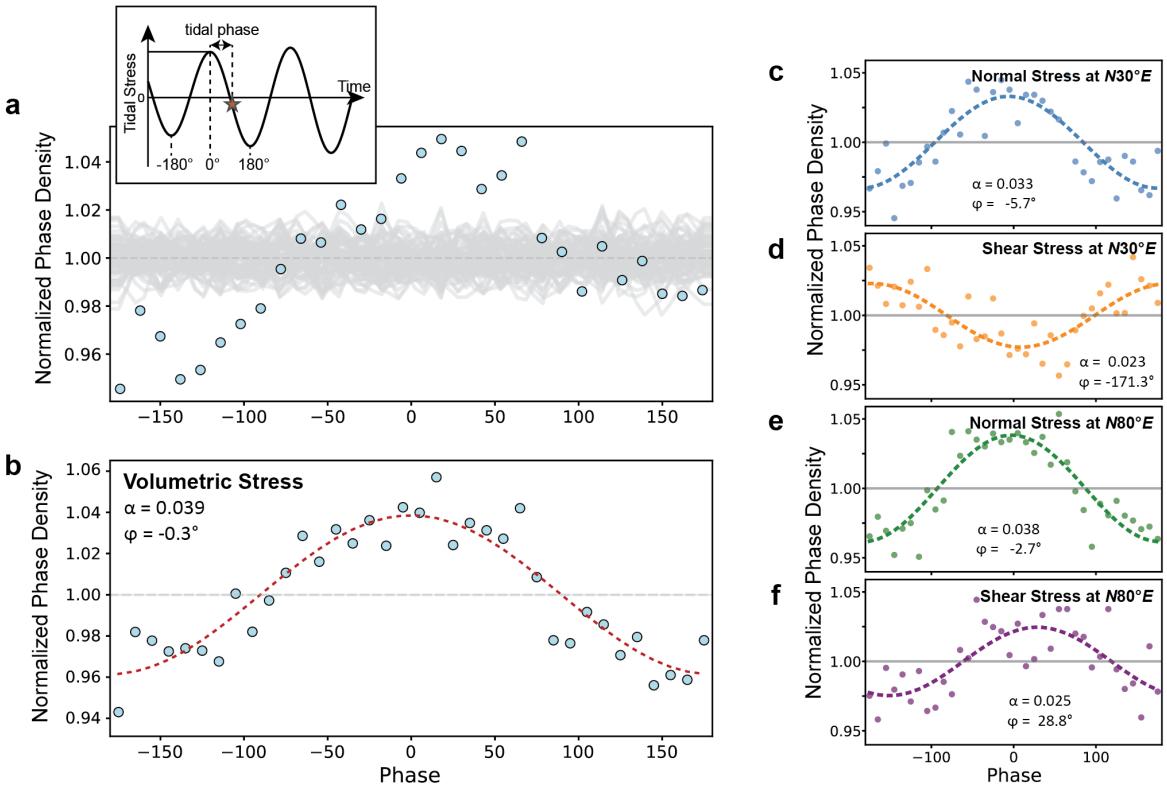


Fig. 2 Illustration of the tidal modulation analysis.
a, Normalized density of event phases (blue dots), defined relative to the full tidal pressure, including constituents of M_2, S_2, N_2, K_2, K_1, O_1, P_1, Q_1, M_f, and M_m. Gray curves show the results for synthetic catalogs with randomized event times (null model), which exhibit no preferred phase. In the schematic tidal stress time series, asterisk is a representative event. Phase is referenced so that 0° corresponds to the peak tidal stress. **b**, Corrected density of event phases (blue dots) after removing the inherent phase bias of the reference signal (see Methods). The red curve is the best–fitting sinusoid used to estimate modulation amplitude and phase. **c-f**, Corrected phase densities computed from normal and shear strain resolved on two groups of steeply dipping fault planes: normal and shear on plane $N30°E$, and normal and shear on plane $N80°E$ [51], respectively.

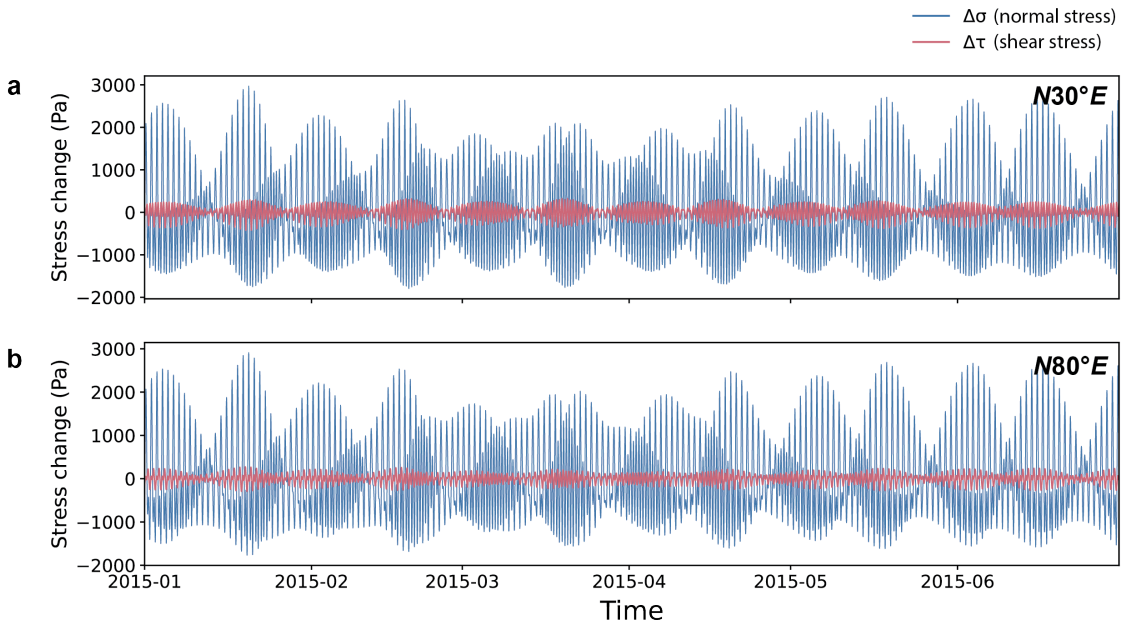


Fig. 3 The decomposition of tidal stress on the two dominant fault planes.
a, Decomposed tidal stress on fault plane I ($N30°E$). **b**, Decomposed tidal stress on fault plane II ($N80°E$). Blue and red line represent the fault normal and shear direction respectively.

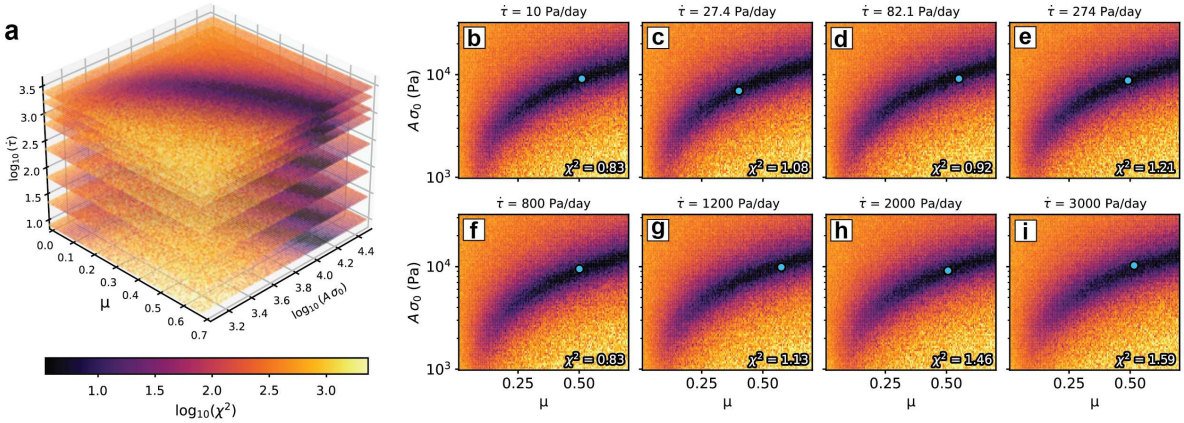


Fig. 4 χ^2 **calculated for different values of** $\dot{\tau}$**,** $A\sigma_0$**, and** mu **under a daily operational pressure change of 700 Pa. a**, χ^2 in 3-D distribution. **b-i**, Each panel shows the slice of χ^2 from the full grid search assuming $\dot{\tau}$ is at specific value. Colors are coded by $log_{10}(\chi^2)$. Blue dots represent the best solved μ and $A\sigma_0$ for each parameter setting.

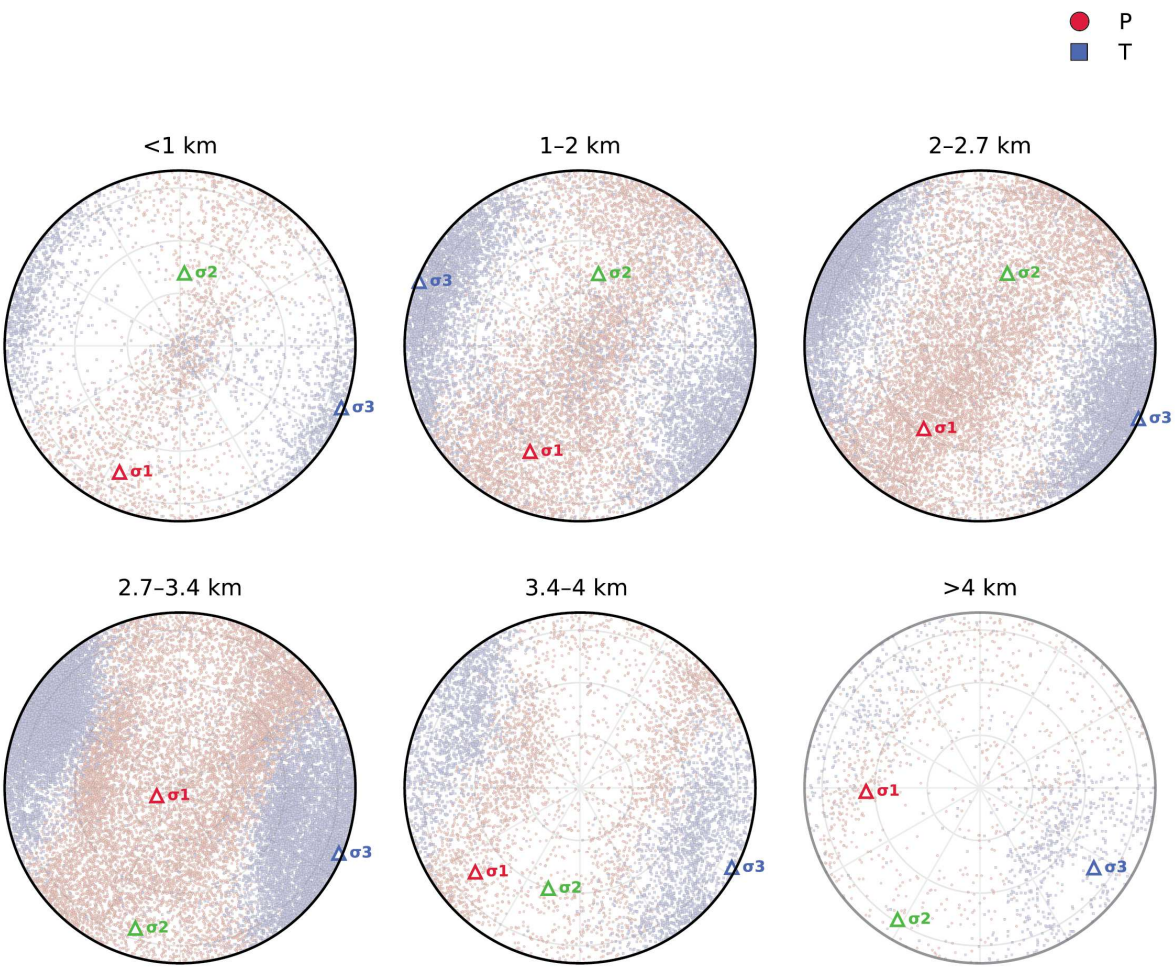


Fig. 5 Stress inversion results (lower-hemisphere projection) for each depth interval.
The solved P- and T-axes are shown as red dots and blue squares, respectively, and the σ_1, σ_2, and σ_3 principal stress axes are indicated by red, green, and blue triangles.

References

[1] Perrey, A.: Sur la fréquence des tremblements de terre relativement à l'âge de la lune pendant la seconde moitié du dix-huitième siècle, et sur la fréquence du phénomène relativement au passage de la lune au méridien. Comptes rendus hebdomadaires des séances de l'Académie des sciences **52**, 146–151 (1861)

[2] Schuster, A.: On lunar and solar periodicities of earthquakes. Proceedings of the Royal Society of London **61**(369-377), 455–465 (1897)

[3] Métivier, L., Viron, O., Conrad, C.P., Renault, S., Diament, M., Patau, G.: Evidence of earthquake triggering by the solid earth tides. Earth and Planetary Science Letters **278**(3-4), 370–375 (2009)

[4] Tanaka, S., Ohtake, M., Sato, H.: Evidence for tidal triggering of earthquakes as revealed from statistical analysis of global data. Journal of Geophysical Research: Solid Earth **107**(B10), 1 (2002)

[5] Zhu, W., Beroza, G.C.: Phasenet: a deep-neural-network-based seismic arrival-time picking method. Geophysical Journal International **216**(1), 261–273 (2019)

[6] Münchmeyer, J.: Pyocto: A high-throughput seismic phase associator. Seismica **3**(1) (2024) https://doi.org/10.26443/seismica.v3i1.1130

[7] Smith, J.D., Azizzadenesheli, K., Ross, Z.E.: Eikonet: Solving the eikonal equation with deep neural networks. IEEE Transactions on Geoscience and Remote Sensing **59**(12), 10685–10696 (2020) https://doi.org/10.1109/TGRS.2020.3039165

[8] Trugman, D.T., Shearer, P.M.: Growclust: A hierarchical clustering algorithm for relative earthquake relocation, with application to the spanish springs and sheldon, nevada, earthquake sequences. Seismological Research Letters **88**(2A), 379–391 (2017) https://doi.org/10.1785/0220160188

[9] Dieterich, J.H.: Earthquake nucleation on faults with rate-and state-dependent strength. Tectonophysics **211**(1-4), 115–134 (1992)

[10] Dieterich, J.: A constitutive law for rate of earthquake production and its application to earthquake clustering. Journal of Geophysical Research: Solid Earth **99**(B2), 2601–2618 (1994)

[11] Heimisson, E.R., Segall, P.: Constitutive law for earthquake production based on rate-and-state friction: Dieterich 1994 revisited. Journal of Geophysical Research: Solid Earth **123**(5), 4141–4156 (2018)

[12] Heimisson, E.R., Avouac, J.-P.: Analytical prediction of seismicity rate due to tides and other oscillating stresses. Geophysical Research Letters **47**(23), 2020–090827 (2020) https://doi.org/10.1029/2020GL090827

[13] Agnew, D.C.: 3.06 earth tides. Treatise on geophysics, 163–195 (2007)

[14] Cochran, E.S., Vidale, J.E., Tanaka, S.: Earth tides can trigger shallow thrust fault earthquakes. Science **306**(5699), 1164–1166 (2004)

[15] Lu, W., Xue, L., Yue, H., Zhuang, J., Zhao, L.: Exploring tidal modulation of seismicity in southern california. Journal of Geophysical Research: Solid Earth **130**(12), 2025–032249 (2025)

[16] Beaucé, E., Poli, P., Waldhauser, F., Holtzman, B., Scholz, C.: Enhanced tidal sensitivity of seismicity before the 2019 magnitude 7.1 ridgecrest, california earthquake. Geophysical Research Letters **50**(14), 2023–104375 (2023)

[17] Zhao, Z., Xue, L., Bürgmann, R., Heimisson, E.R., Lu, W., Yue, H.: Tidal and hydrological seismicity modulations reveal pore fluid diffusion during earthquake nucleation. Science Advances **11**(49), 6350 (2025)

[18] Yan, R., Chen, X., Sun, H., Xu, J., Zhou, J.: A review of tidal triggering of global earthquakes. Geodesy and Geodynamics **14**(1), 35–42 (2023)

[19] Beeler, N., Lockner, D.: Why earthquakes correlate weakly with the solid earth tides: Effects of periodic stress on the rate and probability of earthquake occurrence. Journal of Geophysical Research: Solid Earth **108**(B8) (2003)

[20] Ader, T.J., Lapusta, N., Avouac, J.-P., Ampuero, J.-P.: Response of rate-and-state seismogenic faults to harmonic shear-stress perturbations. Geophysical Journal International **198**(1), 385–413 (2014)

[21] Acosta, M., Avouac, J.-P., Smith, J.D., Sirorattanakul, K., Kaveh, H., Bourne, S.J.: Earthquake nucleation characteristics revealed by seismicity response to seasonal stress variations induced by gas production at groningen. Geophysical Research Letters **50**(19), 2023–105455 (2023)

[22] Brinkman, B.A., LeBlanc, M., Ben-Zion, Y., Uhl, J.T., Dahmen, K.A.: Probing failure susceptibilities of earthquake faults using small-quake tidal correlations. Nature communications **6**(1), 6157 (2015)

[23] Colledge, M., Aubry, J., Chanard, K., Pétrélis, F., Duverger, C., Bollinger, L., Schubnel, A.: Susceptibility of microseismic triggering to small sinusoidal stress perturbations at the laboratory scale. Journal of Geophysical Research: Solid Earth **128**(4), 2022–025583 (2023)

[24] Delorey, A.A., Elst, N.J., Johnson, P.A.: Tidal triggering of earthquakes suggests poroelastic behavior on the san andreas fault. Earth and Planetary Science Letters **460**, 164–170 (2017)

[25] Chanard, K., Nicolas, A., Hatano, T., Petrelis, F., Latour, S., Vinciguerra, S., Schubnel, A.: Sensitivity of acoustic emission triggering to small pore pressure cycling perturbations during brittle creep. Geophysical Research Letters **46**(13), 7414–7423 (2019)

[26] Wang, W., Shearer, P.M., Vidale, J.E., Xu, X., Trugman, D.T., Fialko, Y.: Tidal modulation of seismicity at the coso geothermal field. Earth and Planetary Science Letters **579**, 117335 (2022)

[27] Delorey, A.A., Chen, T.: Behavior of tidally triggered earthquakes depends on fluid conditions. Bulletin of the Seismological Society of America **112**(6), 2890–2901 (2022)

[28] Thomas, A.M., Nadeau, R.M., Bürgmann, R.: Tremor-tide correlations and near-lithostatic pore pressure on the deep san andreas fault. Nature **462**(7276), 1048–1051 (2009)

[29] Ide, S., Tanaka, Y.: Controls on plate motion by oscillating tidal stress: Evidence from deep tremors in western japan. Geophysical Research Letters **41**(11), 3842–3850 (2014)

[30] Houston, H.: Low friction and fault weakening revealed by rising sensitivity of tremor to tidal stress. Nature Geoscience **8**(5), 409–415 (2015)

[31] Beeler, N.M., Thomas, A., Bürgmann, R., Shelly, D.: Constraints on friction, dilatancy, diffusivity, and effective stress from low-frequency earthquake rates on the deep san andreas fault. Journal of Geophysical Research: Solid Earth **123**(1), 583–605 (2018)

[32] Xue, L., Bürgmann, R., Zhao, Z., Beeler, N.M., Heimisson, E.R., Shelly, D.R.: Probing lower-crustal fault properties with frequency-dependent tidal tremor triggering. Earth and Planetary Science Letters **666**, 119480 (2025)

[33] Vergos, G., Arabelos, D., Contadakis, M.: Evidence for tidal triggering on the earthquakes of the hellenic arc, greece. Physics and Chemistry of the Earth, Parts A/B/C **85**, 210–215 (2015)

[34] Bhatnagar, T., Tolstoy, M., Waldhauser, F.: Influence of fortnightly tides on earthquake triggering at

the east pacific rise at 9°50′n. Journal of Geophysical Research: Solid Earth **121**(3), 1262–1279 (2016) https://doi.org/10.1002/2015JB012388

[35] Tan, Y.J., Tolstoy, M., Waldhauser, F., Bohnenstiehl, D.R.: Tidal triggering of microearthquakes over an eruption cycle at 9 50'n east pacific rise. Geophysical Research Letters **45**(4), 1825–1831 (2018)

[36] Zheng, J., Wang, W., Zhang, J.: Detecting tidal periodicities of earthquake occurrence in japan using spectral analyses. Seismological Research Letters **96**(4), 2504–2511 (2025)

[37] Vidale, J.E., Agnew, D.C., Johnston, M.J., Oppenheimer, D.H.: Absence of earthquake correlation with earth tides: An indication of high preseismic fault stress rate. Journal of Geophysical Research: Solid Earth **103**(B10), 24567–24572 (1998)

[38] Petrosino, S., Dumont, S., Morabito, S., Cusano, P.: Tidal and environmental modulation of seismic noise at mefite d'ansanto (italy) non-volcanic co2 emission field. Frontiers in Earth Science **13**, 1708254 (2025)

[39] Johnson, L.R., Majer, E.L.: Induced and triggered earthquakes at the geysers geothermal reservoir. Geophysical Journal International **209**(2), 1221–1238 (2017)

[40] Majer, E.L., Peterson, J.E.: The impact of injection on seismicity at the geysers, california geothermal field. International Journal of Rock Mechanics and Mining Sciences **44**(8), 1079–1090 (2007)

[41] Kwiatek, G., Martínez-Garzón, P., Dresen, G., Bohnhoff, M., Sone, H., Hartline, C.: Effects of long-term fluid injection on induced seismicity parameters and maximum magnitude in northwestern part of the geysers geothermal field. Journal of Geophysical Research: Solid Earth **120**(10), 7085–7101 (2015)

[42] Martínez-Garzón, P., Zaliapin, I., Ben-Zion, Y., Kwiatek, G., Bohnhoff, M.: Comparative study of earthquake clustering in relation to hydraulic activities at geothermal fields in california. Journal of Geophysical Research: Solid Earth **123**(5), 4041–4062 (2018)

[43] Julian, B.R., Ross, A., Foulger, G.R., Evans, J.R.: Threedimensional seismic image of a geothermal reservoir: The geysers, california. Geophysical Research Letters **23**(6), 685–688 (1996) https://doi.org/10.1029/95GL03321

[44] Garcia, J., Hartline, C., Walters, M., Wright, M., Rutqvist, J., Dobson, P.F., Jeanne, P.: The northwest geysers egs demonstration project, california: Part 1: characterization and reservoir response to injection.

Geothermics **63**, 97–119 (2016)

[45] Oppenheimer, D.H.: Extensional tectonics at the geysers geothermal area, california. Journal of Geophysical Research: Solid Earth **91**(B11), 11463–11476 (1986)

[46] Ross, A., Foulger, G.R., Julian, B.R.: Non-double-couple earthquake mechanisms at the geysers geothermal area, california. Geophysical Research Letters **23**(8), 877–880 (1996) https://doi.org/10.1029/96GL00590

[47] Martínez-Garzón, P., Bohnhoff, M., Kwiatek, G., Dresen, G.: Stress tensor changes related to fluid injection at the geysers geothermal field, california. Geophysical Research Letters **40**(11), 2596–2601 (2013)

[48] Guilhem, A., Hutchings, L., Dreger, D.S., Johnson, L.R.: Moment tensor inversions of $m \sim 3$ earthquakes in the geysers geothermal field, california. Journal of Geophysical Research: Solid Earth **119**(3), 2121–2137 (2014) https://doi.org/10.1002/2013JB010271

[49] Ader, T.J., Avouac, J.-P.: Detecting periodicities and declustering in earthquake catalogs using the schuster spectrum, application to himalayan seismicity. Earth and Planetary Science Letters **377**, 97–105 (2013)

[50] Martínez-Garzón, P., Kwiatek, G., Sone, H., Bohnhoff, M., Dresen, G., Hartline, C.: Spatiotemporal changes, faulting regimes, and source parameters of induced seismicity: A case study from the geysers geothermal field. Journal of Geophysical Research: Solid Earth **119**(11), 8378–8396 (2014)

[51] Boyle, K., Zoback, M.: The stress state of the northwest geysers, california geothermal field, and implications for fault-controlled fluid flow. Bulletin of the Seismological Society of America **104**(5), 2303–2312 (2014)

[52] Johnson, C.W., Totten, E.J., Bürgmann, R.: Depth migration of seasonally induced seismicity at the geysers geothermal field. Geophysical Research Letters **43**(12), 6196–6204 (2016)

[53] Page, M.T., Elst, N.J., Hainzl, S.: Testing rate-and-state predictions of aftershock decay with distance. Seismological Research Letters **95**(6), 3376–3386 (2024)

[54] Norbeck, J., Rubinstein, J.L.: Hydromechanical earthquake nucleation model forecasts onset, peak, and falling rates of induced seismicity in oklahoma and kansas. Geophysical Research Letters **45**(7),

2963–2975 (2018)

[55] Marty, S., Avouac, J., Langenbruch, C., Curry, W.: Coulomb stress-based forecasting of injection-induced seismicity in oklahoma and kansas. Earth and Planetary Science Letters **671**, 119677 (2025)

[56] Acworth, R., Brain, T.: Calculation of barometric efficiency in shallow piezometers using water levels, atmospheric and earth tide data. Hydrogeology Journal **16**(8), 1469–1481 (2008)

[57] Marone, C.: Laboratory-derived friction laws and their application to seismic faulting. Annual Review of Earth and Planetary Sciences **26**(1), 643–696 (1998)

[58] Beeler, N., Tullis, T., Weeks, J.: The roles of time and displacement in the evolution effect in rock friction. Geophysical research letters **21**(18), 1987–1990 (1994)

[59] Williamson, K.: Reservoir simulation of the geysers geothermal field. In: Proceedings Fifteen Workshop on Geothermal Reservoir Engineering, Stanford University (1990)

[60] Gunasekera, R.C., Foulger, G.R., Julian, B.R.: Reservoir depletion at the geysers geothermal area, california, shown by four-dimensional seismic tomography. Journal of Geophysical Research: Solid Earth **108**(B3) (2003)

[61] Sirorattanakul, K., Ross, Z.E., Khoshmanesh, M., Cochran, E.S., Acosta, M., Avouac, J.-P.: The 2020 westmorland, california earthquake swarm as aftershocks of a slow slip event sustained by fluid flow. Journal of Geophysical Research: Solid Earth **127**(11), 2022–024693 (2022)

[62] Johnson, C.W., Fu, Y., Bürgmann, R.: Seasonal water storage, stress modulation, and california seismicity. Science **356**(6343), 1161–1164 (2017)

[63] Hawthorne, J.C., Rubin, A.M.: Tidal modulation of slow slip in cascadia. Journal of Geophysical Research: Solid Earth **115**(B9) (2010)

[64] Byerlee, J.: Friction of rocks. Pure and applied geophysics **116**(4), 615–626 (1978)

[65] Scholz, C.H.: Earthquakes and friction laws. Nature **391**(6662), 37–42 (1998)

[66] Beeler, N., Simpson, R., Hickman, S., Lockner, D.: Pore fluid pressure, apparent friction, and coulomb failure. Journal of Geophysical Research: Solid Earth **105**(B11), 25533–25542 (2000)

[67] Wang, H.F.: Theory of Linear Poroelasticity with Applications to Geomechanics and Hydrogeology.

Princeton University Press, Princeton, NJ (2000)

[68] Obara, K.: Nonvolcanic deep tremor associated with subduction in southwest japan. Science **296**(5573), 1679–1681 (2002)

[69] Shelly, D.R., Beroza, G.C., Ide, S., Nakamula, S.: Low-frequency earthquakes in shikoku, japan, and their relationship to episodic tremor and slip. Nature **442**(7099), 188–191 (2006)

[70] Wilcock, W.S.: Tidal triggering of earthquakes in the northeast pacific ocean. Geophysical Journal International **179**(2), 1055–1070 (2009)

[71] Trugman, D.T., Shearer, P.M., Borsa, A.A., Fialko, Y.: A comparison of long-term changes in seismicity at the geysers, salton sea, and coso geothermal fields. Journal of Geophysical Research: Solid Earth **121**(1), 225–247 (2016)

[72] Rutqvist, J., Jeanne, P., Dobson, P.F., Garcia, J., Hartline, C., Hutchings, L., Singh, A., Vasco, D.W., Walters, M.: The northwest geysers egs demonstration project, california–part 2: Modeling and interpretation. Geothermics **63**, 120–138 (2016) https://doi.org/10.1016/j.geothermics.2015.08.002

[73] Martínez-Garzón, P., Kwiatek, G., Bentz, S., Bohnhoff, M., Dresen, G.: Induced earthquake potential in geothermal reservoirs: Insights from the geysers, california. The Leading Edge **39**(12), 873–882 (2020)

[74] Smith, J.D., Ross, Z.E., Azizzadenesheli, K., Muir, J.B.: Hyposvi: Hypocentre inversion with stein variational inference and physics-informed neural networks. Geophysical Journal International **228**(1), 698–710 (2022)

[75] Wilding, J.D., Zhu, W., Ross, Z.E., Jackson, J.M.: The magmatic web beneath hawai'i. Science **379**(6631), 462–468 (2023) https://doi.org/10.1126/science.ade5755

[76] U.S. Geological Survey, Earthquake Hazards Program: Advanced National Seismic System (ANSS) Comprehensive Catalog (ComCat) of Earthquake Events and Products. https://doi.org/10.5066/F7MS3QZH

[77] Richter, C.F.: An instrumental earthquake magnitude scale. Bulletin of the Seismological Society of America **25**(1), 1–32 (1935)

[78] Hutton, L.K., Boore, D.M.: The M_L scale in southern california. Bulletin of the Seismological Society of America **77**(6), 2074–2094 (1987) https://doi.org/10.1785/BSSA0770062074

[79] Uhrhammer, R.A., Collins, E.R.: Synthesis of wood–anderson seismograms from broadband digital records. Bulletin of the Seismological Society of America **80**(3), 702–716 (1990)

[80] Miao, Q., Langston, C.A.: Empirical distance attenuation and the local-magnitude scale for the central united states. Bulletin of the Seismological Society of America **97**(6), 2137–2151 (2007) https://doi.org/10.1785/0120060188

[81] Menke, W.: Geophysical Data Analysis: Discrete Inverse Theory, 4th edn. Academic Press, ??? (2018)

[82] Zaliapin, I., Ben-Zion, Y.: Earthquake clusters in southern california i: Identification and stability. Journal of Geophysical Research: Solid Earth **118**(6), 2847–2864 (2013)

[83] Rubinstein, R.Y., Kroese, D.P.: Simulation and the Monte Carlo Method, 3rd edn. Wiley Series in Probability and Statistics. John Wiley & Sons, Hoboken, NJ (2016)

[84] Linker, M., Dieterich, J.H.: Effects of variable normal stress on rock friction: Observations and constitutive equations. Journal of Geophysical Research: Solid Earth **97**(B4), 4923–4940 (1992)

[85] Daley, D.J., Vere-Jones, D.: An Introduction to the Theory of Point Processes: Volume I: Elementary Theory and Methods. Springer, ??? (2003)

[86] Wilding, J.D., Ross, Z.E.: Insights on the state of stress in the mantle beneath pahala, hawai'i. Volcanica **7**(1), 1–19 (2024) https://doi.org/10.30909/vol.07.01.0119

[87] Shearer, P.M., Prieto, G.A., Hauksson, E.: Comprehensive analysis of earthquake source spectra in southern california. Journal of Geophysical Research: Solid Earth **111**(B6), 06303 (2006) https://doi.org/10.1029/2005JB003979

[88] Trugman, D.T., Shearer, P.M.: Application of an improved spectral decomposition method to examine earthquake source scaling in southern california. Journal of Geophysical Research: Solid Earth **122**(4), 2890–2910 (2017)

[89] Trugman, D.T., Ross, Z.E., Johnson, P.A.: Imaging stress and faulting complexity through earthquake waveform similarity. Geophysical Research Letters **47**(1), 2019–085888 (2020) https://doi.org/10.1029/2019GL085888

[90] Kwiatek, G., Martínez-Garzón, P., Bohnhoff, M.: Hybridmt: A matlab/shell environment package for seismic moment tensor inversion and refinement. Seismological Research Letters **87**(4), 964–976 (2016)

https://doi.org/10.1785/0220150251

[91] Fitch, T.J., McCowan, D.W., Shields, M.W.: Estimation of the seismic moment tensor from teleseismic body wave data with applications to intraplate and mantle earthquakes. Journal of Geophysical Research: Solid Earth **85**(B7), 3817–3828 (1980) https://doi.org/10.1029/JB085iB07p03817

[92] Liu, Q., Wang, D.: Stein variational gradient descent: A general purpose Bayesian inference algorithm. In: Advances in Neural Information Processing Systems (NeurIPS), vol. 29. Curran Associates, Inc., ??? (2016)

[93] Huber, P.J.: Robust estimation of a location parameter. Annals of Mathematical Statistics **35**(1), 73–101 (1964)

[94] Frohlich, C.: Display and quantitative assessment of distributions of earthquake focal mechanisms. Geophysical Journal International **144**(2), 300–308 (2001)

Supplementary Files

This is a list of supplementary files associated with this preprint. Click to download.

- supplement.pdf